Chapter 10

Muon Arm

10.1 Overview

The PHENIX muon arm is designed to give PHENIX acceptance for particles decaying into lepton pairs emitted at rapidities away from $y = 0$. The angular distribution of final-state particles increases rapidly away from $y = 0$, increasing as approximately $1/\sin^2(\theta)$ for a flat rapidity distribution. Detecting e^+e^- pairs becomes difficult in this environment, whereas detecting $\mu^+\mu^-$ pairs remains technically feasbile, provided that the absorber material used to remove hadrons is thin enough to preserve sufficient mass resolution for the $\mu^+\mu^-$ pairs. The mass resolution for the PHENIX muon arm is sufficient to resolve the ϕ from the $\rho+\omega$, the ψ' from the J/ψ, and the $\Upsilon(2S+3S)$ from the $\Upsilon(1S)$, as was mentioned in Chapter 3.

An elevation view of the PHENIX muon arm and its relation to the PHENIX central magnet and the RHIC major facility hall is shown in Fig. 10.1. A summary of channel counts is given in Table 10.1.

The muon arm covers polar angles $10° \leq \theta \leq 35°$. The limits to polar angle coverage result from the size of the piston in the muon magnet at small polar angles and the need to clear the RICH focal plane array at large polar angles. The arm has nearly full azimuthal

Table 10.1: Summary of Channel Counts for Muon Arm

Detector	Layer #	# Channels
μT	1	4416
Station	2	5520
	3	9744
	Total	19,680
μID	1	1536
Plane	2	1536
	3	1536
	Total	4608

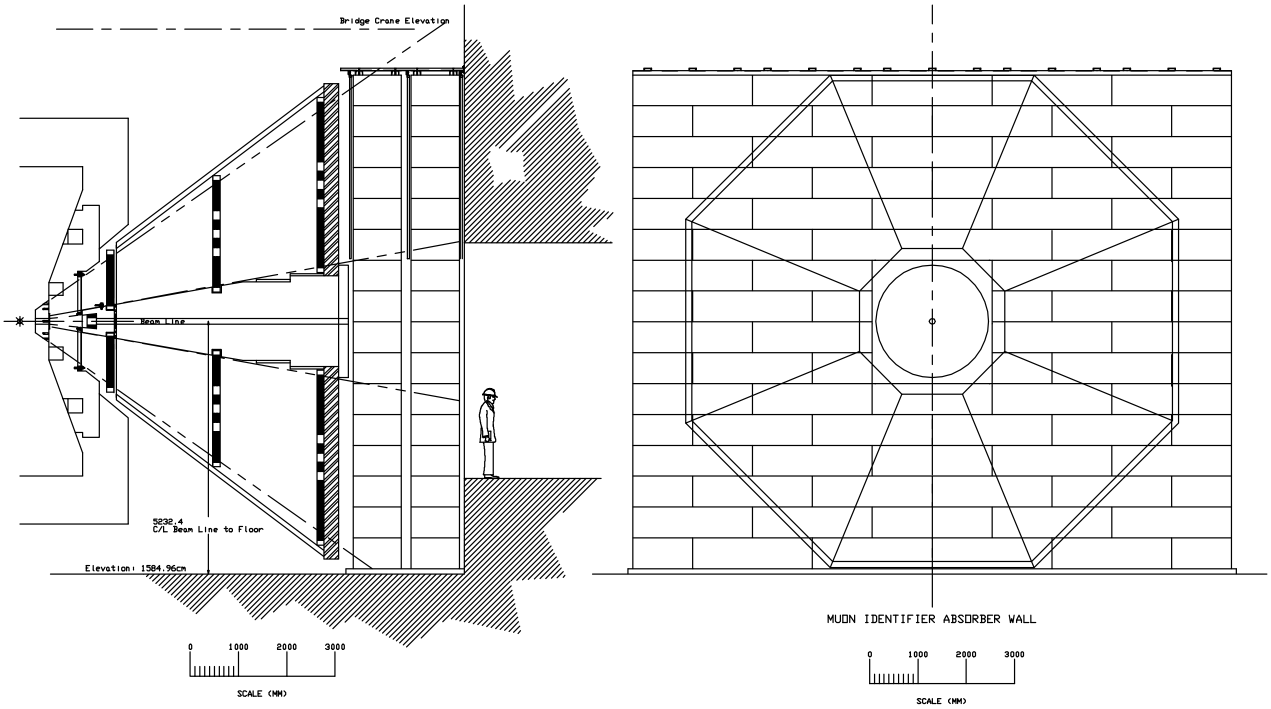

Figure 10.1: Elevation view of PHENIX muon arm in the major facility hall.

angle coverage. The tracking chambers are separated into octagonal sections for construction and handling reasons, resulting in some azimuthal dead space caused by the radial parts of the chamber support frames.

The hadron flux entering the muon arm is reduced to a manageable level by the main mass of steel in the central and muon magnets and several specialized absorbers. The placement of these around the magnet yoke is shown in Fig. 10.2. A copper nosecone is added to the central magnet pole tip to shorten the distance from the interaction vertex to the absorber in order to reduce the number of muons from weak decays of hadrons. A copper plug is added behind the central magnet pole, surrounding one set of beam-beam counters, to reduce leakage from showers caused by forward angle hadrons. A lead curtain is added after the central magnet steel to cut down on soft electromagnetic products of showers. The results of the shower leakage calculations are presented in Section 10.4.1 and the absorber engineering designs are in Section 10.2.2.

Charged particles entering the muon arm are tracked by three stations of multi-plane drift chambers. Each station has six planes and three stereo views. These chambers must deliver position resolution per station better than 150 μm, as discussed below in Section 10.4.2. The third station is more than 4 m in radius, which led to subdivision of the tracking stations into octants in azimuth. Further discussion is given in Section 10.2.3.

The design of the muon arm deliberately has the absorber sections as thin as possible consistent with keeping the tracking chamber occupancies low enough to perform pattern

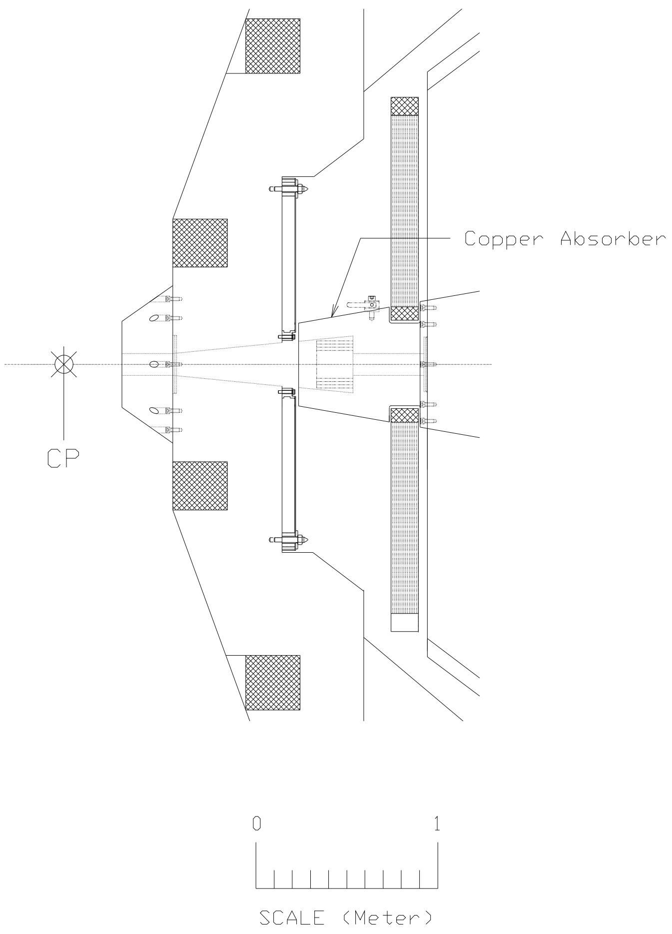

Figure 10.2: View of muon arm region surrounding the beam-beam counters.

recognition and obtain acceptable position resolution. Such an absorber does not provide sufficient hadron rejection for the "muon" sample, so a final detector section provides the needed additional hadron rejection. This detector, called the muon identifier, consists of three large walls of inert absorber interleaved with layers of limited streamer tubes of the Iarocci type. The streamer tubes are instrumented with two sets of pickup pads to give low resolution tracking capability and provide signals corresponding to a useful geometrical segmentation to the first level muon trigger. The first absorber wall is the steel endplate flux return of the muon magnet, and the other two are made of stacked concrete block. The performance of the muon identifier is described in Section 10.4.3 and its design is presented in Section 10.2.4.

Some considerations about triggering the muon arm are given in Section 10.3. The overall performance is addressed briefly in Chapter 3, with particulars given in Section 10.4.4.

Cost and schedule information are given in Sections 10.5 and 10.6, respectively.

10.1.1 Acceptance and Coverage

The main purpose of the muon detector is to detect muon pairs originating from vector meson decay or virtual photon production. This section will focus on the detector performance for simple events consisting only of a correlated pair of oppositely charged muons. All dimuon events have been generated with event generators based on Vogt's parameterizations [1] of the production cross sections for the vector meson resonances in heavy ion reactions, and their rapidity and p_T distributions. The results presented assume a muon energy threshold of 2 GeV, which corresponds to a muon energy sufficient to penetrate to the deepest layer of the muon identifier. A lower muon threshold would be attained by including muons which penetrate through the second absorber layer only.

The geometrical acceptance, assuming uniform distributions in rapidity and p_T, for the ρ, ϕ, J/ψ, and Υ is shown in Fig. 10.3. The effect of the 2 GeV muon threshold is seen as a cutoff at low transverse momentum for the lighter mass vector mesons. The cutoff appears at a transverse mass of around 2–3 GeV/c^2. The transverse momentum cutoff decreases at forward rapidity due to the boost received.

The rapidity and p_T dependence of the acceptance, for vector mesons emitted into the muon detector aperture, is illustrated in Fig. 10.4. The acceptances of the J/ψ and the Υ are bell-shaped in rapidity between 1.1 and 2.6 with a maximum of about 50% at $y = 1.9$. The acceptance is nearly constant as a function of p_T; the structure in the J/ψ acceptance suggested in Fig. 10.3 is masked by statistical fluctuations in the high p_T region. For the low mass ϕ resonance the acceptance is, however, more restricted. The rapidity acceptance is dominantly in the interval from 1.8–2.4, with a maximum of 6 % at $y = 2.2$. The p_T acceptance is reduced in the interval from 0.0–1.5 GeV/c by the muon momentum threshold (the apparent cutoff at large p_T is only due to limited statistics in the simulation). The difference in the ϕ rapidity acceptance between Figs. 10.3 and 10.4 arises from folding the geometrical acceptance with the p_T spectrum of the ϕ, which heavily weights the low p_T region.

The total acceptance, integrated over the expected rapidity and transverse momentum distributions is 0.13%, 0.38%, 5.4%, and 5.9% for the ρ, ϕ, J/ψ, and Υ, respectively. The integrated acceptance decreases rapidly with decreasing mass due to the transverse mass cutoff resulting from the momentum threshold of the spectrometer (see Fig. 10.3).

The rapidity and p_T acceptance of Drell-Yan (DY) produced dimuons is similar to the heavy vector meson acceptance as illustrated in Fig. 10.5. The mass dependence of the acceptance of DY shows the usual steep decrease for masses lower than 3 GeV/c^2, but only a slow decrease for masses larger than 4 GeV/c^2. The maximum acceptance for DY in x_F is around 0.25 with a total acceptance interval of $0.05 < x_F < 0.6$.

A major background source is muons (and electrons) from decay of D and $\bar{\mathrm{D}}$ resonances. In Figs. 10.6 and 3.7, the acceptances for dimuon pairs and muon-electron pairs from charm decays, respectively, are shown. For $\mathrm{D}\bar{\mathrm{D}} \rightarrow \mu^+ + \mu^- + X$, with both muons detected by the muon spectrometer, the acceptance is similar to that for DY. The acceptance for $\mathrm{D}\bar{\mathrm{D}} \rightarrow \mathrm{e} + \mu + \mathrm{X}$ is considerably different however, since the electron is detected by the central electron detector and the muon by the endcap muon detector. In this case, the rapidity coverage stretches from 0.0 to 1.6 with a maximum of 0.5% at $y = 0.8$. The

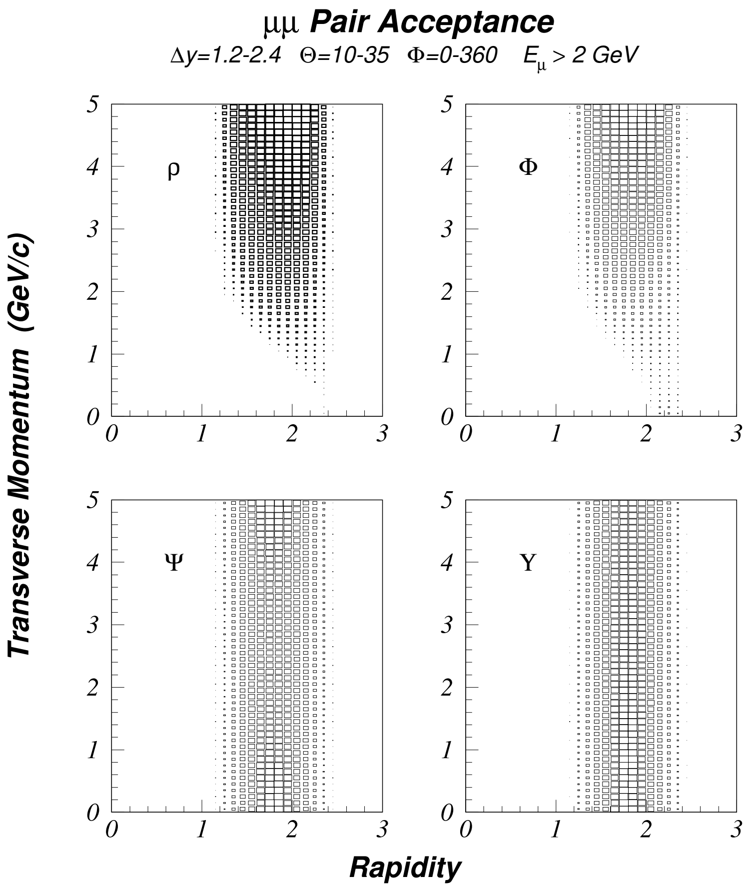

Figure 10.3: Geometrical acceptance in rapidity versus transverse momentum for the ρ, ϕ, J/ψ, and Υ.

pair mass acceptance vanishes below 2 GeV/c^2, steeply increases from 2 to 4 GeV/c^2 and is essentially constant above 4 GeV/c^2. The large fluctuations in Fig. 3.7b at large pair masses are caused by low statistics. The x_F coverage is between 0.0 and 0.22, with a maximum at 0.08.

The advantages of detecting dileptons to obtain information on the hot and dense phase of high energy nuclear collisions have been extensively discussed. The disadvantage of using nonstrongly interacting probes is the much smaller cross sections and yields. In the following, we will address the crucial question of the expected yields of the vector mesons in the muon detector. It is important to note that the large acceptance of the muon arm provides a significantly larger rate than the electron measurement for higher mass dileptons, and the two measurements are complementary in mass as well as rapidity range.

All cross section estimates are based on the observation that hadro-production of vector